

Constructing the frequency and wave normal distribution of whistler-mode wave power

C. E. J. Watt,¹ A. W. Degeling,¹ and R. Rankin¹

Received 21 December 2012; revised 7 March 2013; accepted 13 March 2013; published 8 May 2013.

[1] We introduce a new methodology that allows the construction of wave frequency distributions due to growing incoherent whistler-mode waves in the magnetosphere. The technique combines the equations of geometric optics (i.e., raytracing) with the equation of transfer of radiation in an anisotropic lossy medium to obtain spectral energy density as a function of frequency and wavenormal angle. We describe the method in detail and then demonstrate how it could be used in an idealized magnetosphere during quiet geomagnetic conditions. For a specific set of plasma conditions, we predict that the wave power peaks off the equator at $\sim 15^\circ$ magnetic latitude. The new calculations predict that wave power as a function of frequency can be adequately described using a Gaussian function, but as a function of wavenormal angle, it more closely resembles a skew normal distribution. The technique described in this paper is the first known estimate of the parallel and oblique incoherent wave spectrum as a result of growing whistler-mode waves and provides a means to incorporate self-consistent wave-particle interactions in a kinetic model of the magnetosphere over a large volume.

Citation: Watt, C. E. J., A. W. Degeling, and R. Rankin (2013), Constructing the frequency and wave normal distribution of whistler-mode wave power, *J. Geophys. Res. Space Physics*, 118, 1984–1991, doi:10.1002/jgra.50231.

1. Introduction

[2] Raytracing of whistler-mode waves through the magnetosphere has promoted further understanding of the propagation of these important waves [e.g., *Inan and Bell*, 1977; *Thorne et al.*, 1979; *Church and Thorne*, 1983; *Huang and Goertz*, 1983; *Huang et al.*, 1983; *Chum et al.*, 2003; *Chum and Santolik*, 2005; *Bortnik et al.*, 2006, 2007a, 2007b, 2008; *Li et al.*, 2008, 2009; *Bortnik et al.*, 2011a]. By combining raytracing and solutions from the linear dispersion relation, the parameters governing the linear behavior of a wave of frequency $\omega = 2\pi f$ can be diagnosed at each step along the ray path: wavenormal angle, ray direction, group time, linear growth rate, and path-integrated gain. The gain of a single wave is not a parameter that is measured by spacecraft, and the wave spectrum at any one point represents the combined gain of many waves with different trajectories and histories. Instead, a more useful quantity is wave energy density as a function of frequency and wavenormal angle, and this is what is often used to drive particle diffusion models [e.g., *Beutier and Boscher*, 1995; *Glauert and Horne*, 2005; *Shprits et al.*, 2008; *Su et al.*, 2010].

[3] Recent work has sought to construct wave power distributions using ray tracing analysis for damped chorus emissions [*Bortnik et al.*, 2011b; *Chen et al.*, 2012a, 2012b, 2013] and growing incoherent whistler-mode waves [*Watt et al.*, 2012]. The challenge for constructing wave frequency distributions is to include all possible contributions to the wave power from all possible ray paths. The first set of studies invokes the assumption that all wave power is emitted at the magnetic equator and then the wave power is mapped to different locations using forward or backward raytracing, modifying the power to account for geometric effects and Landau damping of the waves [*Bortnik et al.*, 2011b; *Chen et al.*, 2012a, 2012b, 2013]. Using a similar method, but with different assumptions, *Watt et al.* [2012] attempted to build up a picture of the incoherent wave-power due to growing whistler-mode waves by tracing tens of millions of raypaths using random initial locations from a region $5 < L < 10$ and $-30^\circ < \lambda < 30^\circ$ and random initial wave parameters selected from the range of unstable frequencies and wave normal angles. The key difference between the two approaches is that *Watt et al.* [2012] make no assumptions regarding source location; waves may be generated anywhere in the magnetosphere where the local plasma conditions support linear whistler-mode wave growth. Nonetheless, the approach of *Watt et al.* [2012] only yields the distribution of wave gain at any particular location. Distributions of wave gain can provide some indication of the wave parameters that encourage the most growth but cannot be compared directly with satellite observations.

[4] In this paper, we describe a technique that estimates spectral energy density from these gains as a function of

¹Department of Physics, University of Alberta, Edmonton, Alberta, Canada.

Corresponding author: C. E. J. Watt, Department of Physics, University of Alberta, Edmonton, AB T6G 2G7, Canada. (watt@ualberta.ca)

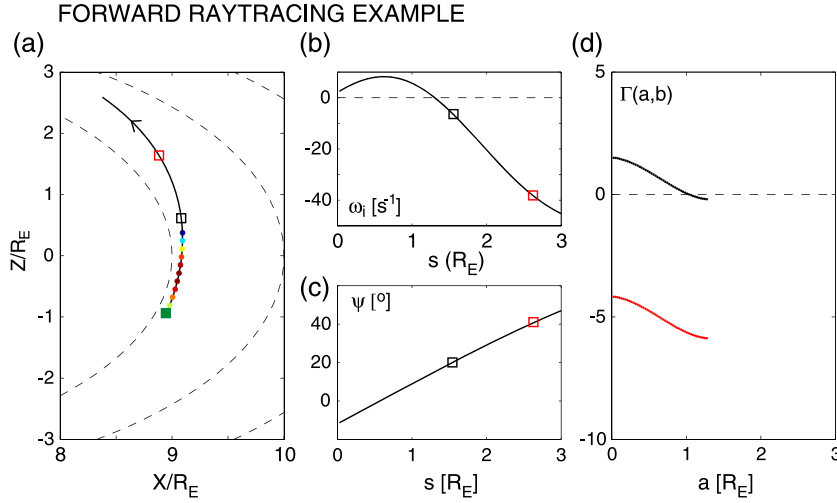


Figure 1. (a) Growing raypath from *Watt et al.* [2012] initialized at radial distance $r = 9R_E$ and magnetic latitude $\lambda = -6^\circ$. Colored dots indicate locations with growth rates $\omega_i > 0$. The arrow indicates ray direction, and the open squares indicate “observation locations.” Dashed lines indicate the dipole magnetic field. (b) Growth rate as a function of distance along the raypath s . (c) Wavenormal angle as a function of s . (d) Path-integrated gain $\Gamma(a, b)$ contributions, where a is a point along s with $\omega_i > 0$, and b is the value of s at the observation location. Values are color coded to match the observation locations in Figure 1a.

frequency and wavenormal angle. Our aim here is to elucidate how to construct the wave frequency distributions for growing incoherent waves; future work will use the technique to investigate wave distributions throughout the magnetosphere for different conditions and investigate the effects that these self-consistent wave distributions have on the resulting electron diffusion.

[5] In section 2, we describe how raytracing and path-integrated gain calculations may be used to construct wave frequency distributions in the magnetosphere. Section 3 presents an example of wave frequency distributions during quiet times as a function of latitude in the model. Examples of wave normal distributions are presented in section 4. We discuss possible uses of these calculations in section 5, before presenting our conclusions in section 6.

2. From Raytracing to Spectral Energy Density

[6] The spectral energy density of waves u_ω in an arbitrary anisotropic medium may be calculated from

$$u_\omega = \int_{4\pi} \frac{I_\omega}{v_g} d\chi \quad (1)$$

where u_ω is measured in joules per cubic meter per frequency interval $d\omega$, I_ω is the intensity of the radiation, v_g is the local group velocity of waves of that frequency, and χ is the angle of the group velocity relative to the magnetic field or ray direction. In this case, we will measure χ relative to the local magnetic field (i.e., χ is the angle between \mathbf{v}_g and \mathbf{B}_0). Note that for the demonstration in this paper, we will ignore any azimuthal propagation of the whistler-mode waves, and so the integration in equation (1) will cover 2π , although it will be straightforward to extend the calculation to three dimensions where χ is a solid angle. The calculation of spectral energy density therefore requires us to find I_ω as a function of group velocity angle. *Watt et al.* [2012] demonstrated that growing incoherent whistler-mode waves

in a dipolar magnetic field have group velocity angles close to the anti-parallel and parallel directions (i.e., $\chi < 10^\circ$). Note, however, that the maximum gains did not occur for propagation that was exactly aligned with the magnetic field, as is expected from local solutions to the dispersion relation.

[7] In an isotropic medium with no emission, absorption, or scattering, the ratio I_ω/n^2 is constant along a ray path, where $n = |\mathbf{n}| = |c\mathbf{k}/\omega|$ is the refractive index of the medium. The appropriate generalization of this ratio for an anisotropic medium is that I_ω/n_r^2 is constant, where n_r is the “ray refractive index” of the medium given by *Bekefi* [1966]:

$$n_r^2 = \left| n^2 \sin \psi \frac{(1 + \nu^2)^{1/2}}{\frac{\partial}{\partial \psi} \left(\frac{\cos \psi + \nu \sin \psi}{(1 + \nu^2)^{1/2}} \right)} \right| \quad (2)$$

Here ψ is wavenormal angle (i.e., the angle between \mathbf{k} and \mathbf{B}_0), and $\nu = (1/n)(\partial n/\partial \psi)_\omega$. By including growth or damping of waves due to interactions with the plasma, the change in I_ω/n_r^2 along the raypath can be written as follows [cf. *Church and Thorne*, 1983]:

$$\frac{d}{ds} \left(\frac{I_\omega}{n_r^2} \right) = 2 \frac{\omega_i}{v_g} \cos \alpha \frac{I_\omega}{n_r^2} \quad (3)$$

where ω_i is the imaginary frequency of the wave and α is the angle between the group velocity vector and the wavenumber vector. The solution to equation (3) gives the value of intensity at point b along the raypath s :

$$\frac{I_\omega(b)}{n_r^2(b)} = \frac{I_\omega(a)}{n_r^2(a)} \exp \left[\int_a^b 2 \frac{\omega_i(s)}{v_g(s)} \cos(\alpha(s)) ds \right] \quad (4)$$

Note that the integral in equation (4) is equivalent to the calculation of path-integrated gain between points a and b :

$$\Gamma(a, b) = \int_a^b -(k_i \cos \alpha) ds = \int_a^b \frac{\omega_i(s)}{v_g(s)} \cos(\alpha(s)) ds, \quad (5)$$

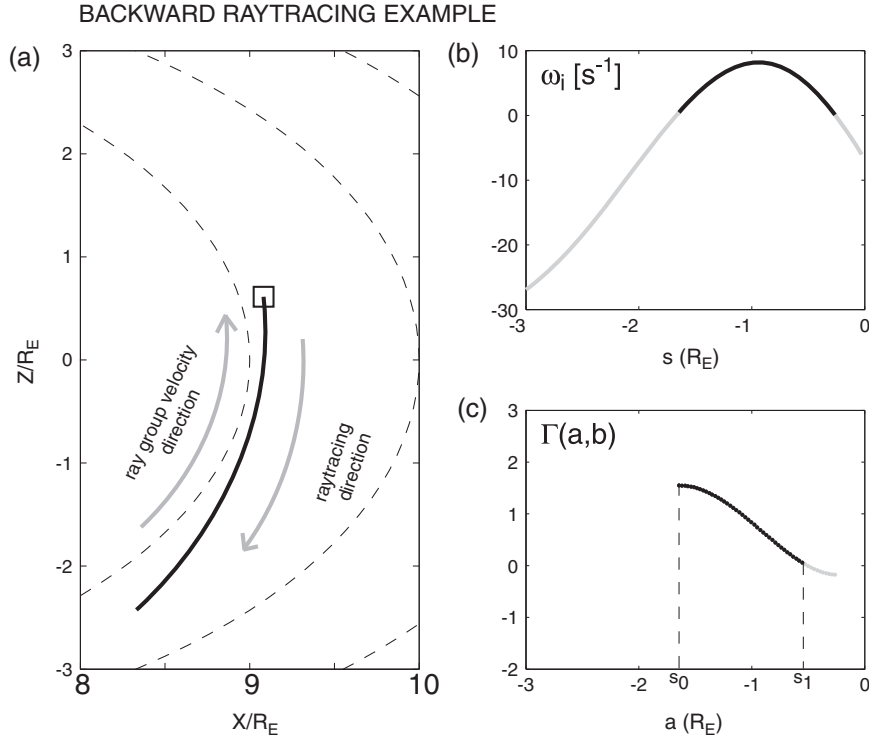


Figure 2. (a) The raypath shown in Figure 1 traced backward from the observation location (open black square). (b) Growth rate ω_i as a function of distance along the path (where $s = 0$ indicates the observation location). The black portion of the curve indicates points along the raypath where waves can grow (i.e., $\omega_i > 0$). (c) The path-integrated gain $\Gamma(a, b)$ calculated at the observation location from each point along s with $\omega_i > 0$. The black dots indicate points along the raypath where both wave growth occurs *and* the resulting path-integrated gain is positive. These points are used to define s_0 and s_1 in equation (10). Gray dots indicate points where the initial ω_i is positive, but the resulting gain is negative.

[cf. *Horne and Thorne, 1997; Watt et al., 2012*] (and note that the factor of 8.6859 required to convert gain to decibel is not required in these calculations). To evaluate the integral in equation (1), we must now find all the intensity contributions from all waves passing through location b .

[8] We will demonstrate our calculations using the same magnetic field and plasma model used by *Watt et al. [2012]*. This study used data from the THEMIS spacecraft published by *Li et al. [2010]* to constrain the choice of plasma parameters. Again, in this paper, we will focus on quiet times ($AE < 100$ nT) and on observations taken outside the plasmasphere at 9MLT as an example of a location where whistler-mode waves are observed.

[9] We construct an idealized dipole model of the magnetospheric magnetic field between $L = 5$ and $L = 10$. A modified diffusive equilibrium model for the electron number density N_e [*Inan and Bell, 1977*], similar to models used by *Bortnik et al. [2006, 2007a, 2007b, 2011a]* is used, with parameters chosen to fit the density profiles shown in *Li et al. [2010]*. The model and the parameters chosen are discussed in detail in the Appendix of *Watt et al. [2012]* and are shown to produce values of $N_e(L)$, and hence the ratio of plasma frequency to gyrofrequency ω_{pe}/Ω_e that matches the variation observed in the statistical THEMIS measurements [*Li et al., 2010, Figure 1b*].

[10] The choice of distribution of warm/hot electrons which provide the plasma instability is also guided by

observations provided in *Li et al. [2010]*. It was found that two warm plasma components, one with $T_{\parallel} = 1.4$ keV and one with $T_{\parallel} = 10$ keV could be used to provide a reasonable fit to the THEMIS survey parameters. Simple functional forms for number density and temperature anisotropy were derived in *Watt et al. [2012]* that describe the variation of these parameters with L . The functions adequately reproduced the statistical survey of anisotropy and phase space density. If $w = (r_{eq}/R_E) - 5$, and r_{eq} is the radial distance at the equator, then the functional forms for populations 1 and 2 in the equatorial plane are as follows:

$$A_{eq,1} = 0.004w^3 + 0.2w \quad (6)$$

$$A_{eq,2} = 0.0061w^3 \quad (7)$$

$$n_{eq,1} = 10^5 + 3.0 \times 10^5 w \quad (8)$$

$$n_{eq,2} = 5.0 \times 10^4 - 8.0 \times 10^3 w \quad (9)$$

The cold plasma density is set equal to $N_e - n_{eq,1} - n_{eq,2}$. The free energy driving the unstable growth of the waves is therefore an electron temperature anisotropy at large values of L .

[11] Figure 1a shows a growing raypath arbitrarily selected from one of the millions of raypaths used in the analysis of *Watt et al. [2012]*. We follow this raypath only for demonstration purposes, before describing later how raypaths will be specially selected to build up the wave distributions. The raypath follows waves with real frequency

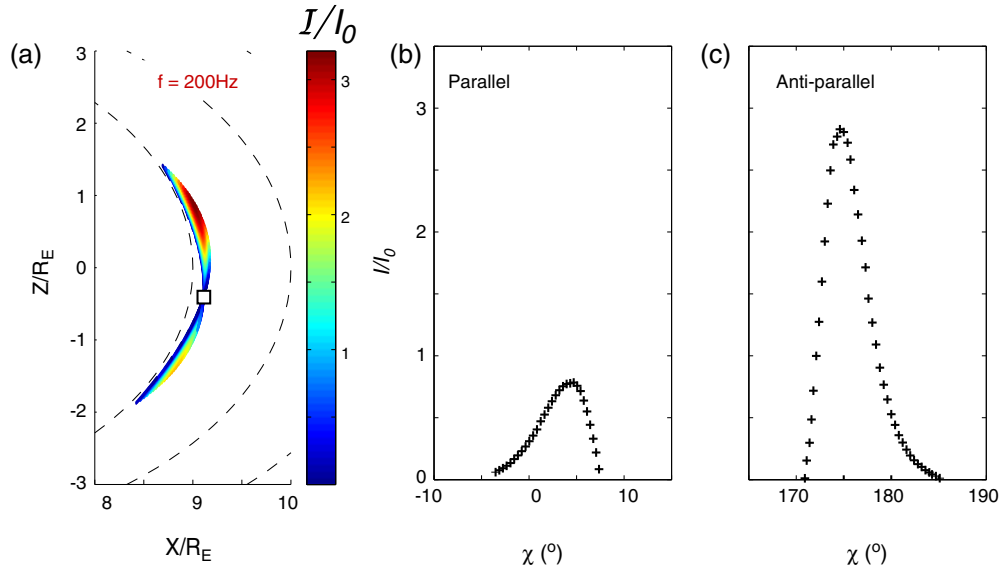


Figure 3. (a) The initialization points of all contributions to wave intensity at the observation location indicated with the open black square; the color indicates the intensity of a wave initialized from that location as it passes through the observation point. (b) Intensity at the observation point as a function of the ray direction χ for parallel waves (i.e., northward traveling waves). (c) Intensity at the observation point as a function of χ for anti-parallel waves (i.e., southward traveling waves).

$f = \omega/(2\pi) = 200$ Hz and initial wavenormal angle $\psi_0 = -11^\circ$ from the initial point at a radial distance $r = 9R_E$ and magnetic latitude $\lambda = -6^\circ$ (indicated by the solid green square). Assuming no azimuthal propagation, the ray path (solid black line) travels northward toward the equator and passes into the northern hemisphere, where it is stopped at an arbitrary location for this demonstration. The arrow on the raypath indicates the ray direction. Indicated with colored dots are locations along the trajectory where the growth rate is positive; warm colors indicate larger growth rates than cooler colors. Figure 1b shows these growth rates as a function of distance s along the path. Growth rates are only positive near the beginning of the raypath, and it is only at these locations that waves can be generated. Imagine an “observation location” along the raypath, where we might wish to construct a wave frequency distribution (indicated with the open black square). The contributions to the wave energy density at $f = 200$ Hz at this location will depend upon how many waves arrive at this location and their path-integrated gain. We calculate the individual $\Gamma(a, b)$ contributions by letting a run through all the points where $\omega_i > 0$ along the path and setting b equal to the value of s at the observation location. The black dots in Figure 1d show these $\Gamma(a, b)$ contributions. Note that the largest gains are contributed by waves that have traveled furthest to arrive at the observation point (i.e., from those waves that started near $s = 0$). Waves that started too near the observation point have negative gain, because they are mostly damped; they will not contribute to u_ω at this frequency. The total contribution from the sum of all incoherent waves generated along this raypath from the arbitrary start point s_0 to the selected observation point is therefore

$$\mathcal{I}(b) = I_0 n_k^2(b) \int_{s_0}^{s_1} \frac{\exp(\Gamma(s, b))}{n_k^2(s)} ds \quad (10)$$

where it is assumed that all waves have the same initial intensity I_0 and s_1 is the last point along the raypath with $\omega_i > 0$ and $\Gamma > 0$.

[12] By choosing an observation point further from the initial point (e.g., the red square in Figure 1a), we can see that there are no contributions to u_ω from any point along the path where $\omega_i > 0$. All values of Γ shown by red dots in Figure 1d are negative.

[13] The arbitrary initialization point used in the traditional forward raytracing displayed in Figure 1a is not the best selection for s_0 in equation (10), and the subsequent raypath is not guaranteed to include all possible contributions from waves along that raypath; there could be points further from the observation point that also have $\omega_i > 0$ and

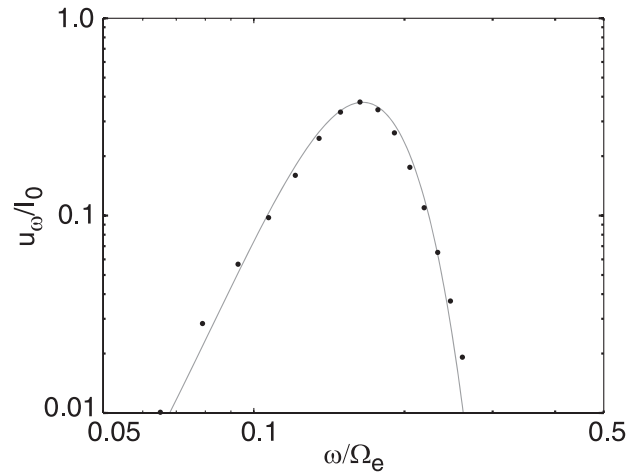


Figure 4. Wave spectral energy density as a function of frequency at $r = 9R_E$ and $\lambda = -6^\circ$. Energy density is normalized to the initial wave intensity.

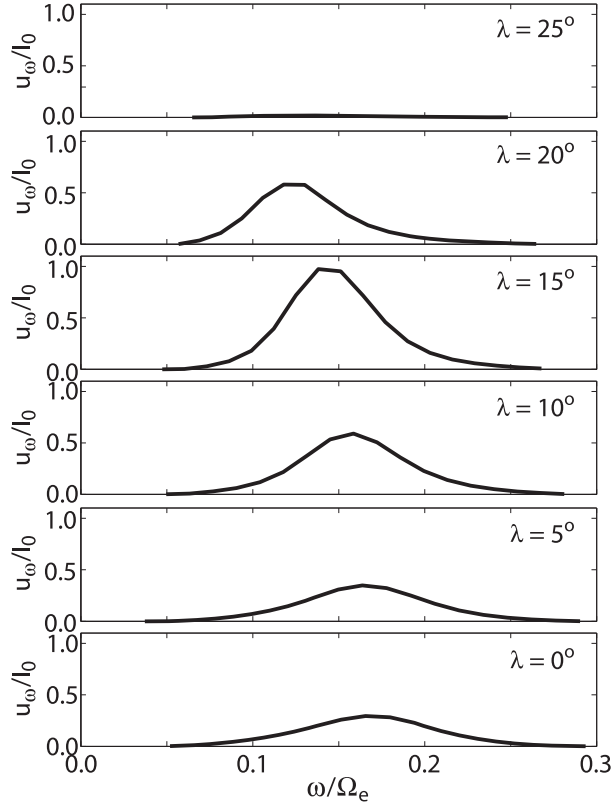


Figure 5. Predicted wave spectral energy density at different latitudes at $L = 9$ for quiet time pre-noon plasma conditions (see *Watt et al.* [2012] for details of the plasma model used in this case).

give $\Gamma > 0$. The best way to include all possible contributions, and therefore establish s_0 and s_1 along each path, is to trace rays *backward* from the observation point. Figure 2 demonstrates how s_0 and s_1 can be chosen using backward raytracing. The same raypath shown in Figure 1 is traced backward from the observation location (open black square). Figure 2b shows the growth rates calculated along the path, where $s = 0$ indicates the observation location. Only at those

points with $\omega_i > 0$ (indicated by the black curve) will waves grow; waves are damped elsewhere (gray curves). The path-integrated gain between each point and the observation point is also calculated (shown in Figure 2c). The black dots indicate those potential ray start points where waves will grow *and* contribute a positive gain at the observation point. The values of s_0 and s_1 can easily be obtained by applying these two conditions.

[14] Equation (1) shows that we must find all raypaths that pass through an observation point at each frequency. We sweep through the wavenormal angle ψ , backtracing rays of constant ω from the observation point to high latitudes. *Watt et al.* [2012] showed that for these plasma conditions, growing paths are confined to $\lambda \pm 30^\circ$ and so backward raypaths are ended once they reach $\lambda \pm 40^\circ$. The process shown in Figure 2 is repeated for each raypath. Some raypaths have no regions of $\omega_i > 0$ and are ignored. Figure 3a shows the color-coded contributions to the intensity $\mathcal{I}(b)$ for $f = 200$ Hz at an observation point 6° south of the equator, calculated using this backward raytracing algorithm. A number of raypaths are shown to contribute to u_ω , with different wavenormals and ray directions at the observation point. The contribution to wave intensity from each path is given by equation (10) and is shown in Figures 3b and 3c as a function of χ , measured clockwise from the magnetic field direction. We will display angles in degrees rather than radians as the angles are quite small. The intensity peaks near the parallel and anti-parallel directions but not directly along the field. It is a simple matter to numerically integrate $\mathcal{I}(\chi)$ as shown in Figures 3b and 3c to obtain u_ω for $f = 200$ Hz.

[15] Figure 4 shows the spectral energy density (normalized to the initial wave intensity I_0) calculated using the backward raytracing technique as a function of normalized frequency at $r = 9R_E$ and $\lambda = -6^\circ$ (the observation point indicated in Figure 3a). It is important to note that the inputs for this model are the form of the magnetic field and the variation in the cold and warm plasma; the waves grow self-consistently according to the free energy in the plasma. For this specific set of conditions, the wave spectrum is narrowly peaked at $f = 200$ Hz and drops off quickly at higher and lower frequencies. Given that all the waves have the same initial intensity I_0 , regardless of frequency or wavenormal

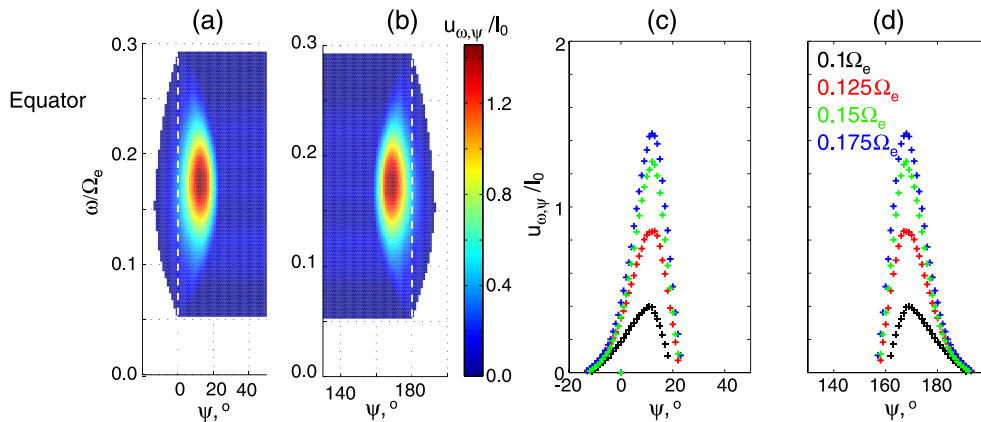


Figure 6. Predicted wavenormal distributions of wave intensity at the equator at $L = 9$: (a) near parallel and (b) near anti-parallel distributions of wave intensity as a function of normalized frequency and wavenormal angle. The white dashed lines indicate the parallel and anti-parallel magnetic field directions; (c and d) cuts through the distribution at four different frequencies.

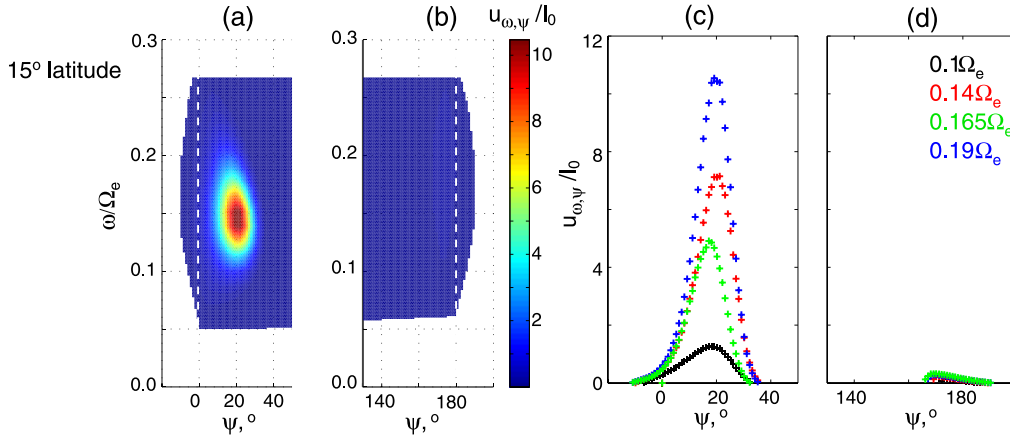


Figure 7. Predicted wavenormal distributions of wave intensity at $L = 9$ and $\lambda = 15^\circ$: (a) near parallel and (b) near anti-parallel distributions of wave intensity as a function of normalized frequency and wavenormal angle. The white dashed lines indicate the parallel and anti-parallel magnetic field directions; (c and d) cuts through the distribution at four different frequencies.

angle, it is very interesting to discover that as a function of frequency only, our prediction of u_ω at this low latitude can be approximated using a Gaussian function:

$$u_\omega \approx A \exp \left[- \left(\frac{(\omega/\Omega_e) - \omega_m}{\delta\omega} \right)^2 \right] \quad (11)$$

where $\omega_m = 0.165$ and $\delta\omega = 0.051$ (indicated by the solid line in Figure 4). It is important to note that the approximately Gaussian distribution of waves near the equator arises naturally from the calculations and is not imposed by active manipulation of wave intensity. We repeat that the only input to the calculations are the choice of plasma model and magnetic field model. Future work will determine whether the functional form of the wave distribution near the equator is a natural consequence of the whistler-mode wave instability, or whether it is controlled by the choice of warm plasma model, or the latitudinal symmetry of the magnetic field model used in the calculations.

3. Wave Frequency Distributions as a Function of Latitude

[16] The creation of wave spectra using the backward raytracing allows us to make a prediction of the relative wave power at different latitudes. Figure 5 shows the predicted variation of wave spectral energy density as a function of magnetic latitude λ at $L = 9$, using the quiet time plasma model described in *Watt et al.* [2012]. The wave power increases from the equator to peak at $\lambda \sim 15^\circ$, before dropping off rapidly at higher latitudes. Near the equator, the wave spectra are approximately Gaussian, but these spectra become more skewed toward lower normalized frequency at higher latitude. Note that the wave frequencies are normalized to the *local* electron gyrofrequency and the local gyrofrequency increases with latitude.

4. Wave Normal Distributions

[17] Figure 6 shows the distribution of normalized wave intensity as a function of wavenormal angle and normalized

frequency at the equator at $L = 9$ using the same quiet time plasma model as before. (The dark blue color in Figures 6a and 6b corresponding to $u_{\omega,\psi}/I_0 = \mathcal{I}/(v_g I_0) = 0$ is an artifact of the interpolation software used to make the surface plot). In agreement with the forward raytracing results of *Watt et al.* [2012], the maximum wave intensity occurs for oblique wavevectors, even at the equator. Figures 6c and 6d show slices through these distributions at constant frequency. The wave intensity distribution is exactly symmetric about $\psi = 90^\circ$ (or $\pi/2$) and more closely resembles a skew normal distribution [O'Hagan and Leonard, 1976] than a Gaussian distribution. It is important to note that our method predicts that wave power near to the equator is a combination of waves traveling in opposite directions. The wavenormal distribution peaks at $\sim 12^\circ$ and $\sim 168^\circ$, where ψ is measured clockwise from the magnetic field direction.

[18] At $\lambda = 15^\circ$ magnetic latitude, the wavenormal distribution has become much less symmetric and peaks at a slightly higher wavenormal angle. Figure 7 shows that the intensity peaks at around $\psi \sim 20^\circ$ and that there is very little wave power with wavenormals pointing toward the equator.

5. Discussion

[19] Predictions of the pitch angle and energy diffusion due to interactions with whistler-mode waves are a vital part of many models of the Earth's radiation belts. Most models incorporate a set of quasilinear diffusion coefficients which are driven by prescribed wave distribution functions as first suggested by *Lyons et al.* [1971]. Many state-of-the-art physics-based models of radiation belt diffusion use this method, e.g., the Salammbô code [Beutier and Boscher, 1995]), the Pitch Angle and Energy Diffusion of Ions and Electrons code (PADIE) [Glauert and Horne, 2005], the Versatile Electron Radiation Belt code (VERB) [Shprits et al., 2008], and the Storm-Time Evolution of Electron Radiation Belt code (STEERB) [Su et al., 2010]. Commonly, the prescribed wave distribution function is separated into two independent Gaussian functions

dependent on frequency and wavenormal angle [e.g., *Glauert and Horne, 2005*]:

$$B^2(\omega) = \begin{cases} A^2 \exp\left(-\frac{(\omega-\omega_m)^2}{\delta\omega^2}\right), & \text{if } \omega_{lc} < \omega < \omega_{uc} \\ 0, & \text{otherwise} \end{cases} \quad (12)$$

$$g(X) = \begin{cases} \exp\left(-\frac{(X-X_m)^2}{X_w^2}\right), & \text{if } X_{\min} < X < X_{\max} \\ 0, & \text{otherwise} \end{cases} \quad (13)$$

where ω_m is the frequency of maximum wavepower, $\delta\omega$ is the frequency width, ω_{lc} and ω_{uc} are the lower and upper frequency cutoffs, $A^2(\omega, \omega_m, \omega_{lc}, \omega_{uc})$ is a normalization constant, $X = \tan \psi$, X_m is the value of X corresponding to maximum wavepower, X_w is the width, and X_{\min} and X_{\max} are the minimum and maximum values of X . The separation of variables in these functions allows for significant mathematical simplification of the calculation of the diffusion coefficients but is not motivated by observations; the exact functional form of $\mathbf{B}^2(\omega, \psi)$ is unknown. Figures 6 and 7 show predictions of this function from a combination of raytracing and solutions to the linear dispersion relation. Although the variation of u_ω with frequency is approximately Gaussian near the equator, at higher latitudes it more closely resembles a skew normal function [*O'Hagan and Leonard, 1976*]. The variation of $u_{\omega, \psi}$ with ψ resembles a skew normal function at all latitudes. Future work will determine whether $u_{\omega, \psi}$ can be best described using two independent functions of ω and ψ or whether the relationship is more complicated.

[20] Quantitative predictions of the wave spectral energy density require an estimate of the original intensity of the waves I_0 . In the absence of other plasma instabilities, the initial intensity of each wave is likely related to the amplitude of the thermal noise in the plasma (see, e.g., *Fejer and Kan, 1969*), and this may vary with frequency and wavenumber. In an inhomogeneous magnetic field, the thermal noise is difficult to calculate from first principles, and so we leave an estimate of I_0 to future work. A more realistic alternative is to validate the predicted wave distributions using in situ observations of incoherent whistler-mode waves. In this way, the initial wave intensity may be calibrated.

[21] An important assumption inherent in the characterization of the wave distributions above (equations (12) and (13)) is that the wave distributions are symmetric with respect to $\pm k_{\parallel}$, or around $\psi = \pi/2$ [*Lyons et al., 1971, Appendix B*]. The linear prediction provided by our raytracing analysis predicts such symmetry only at the equator; at higher latitudes, the wave distributions are skewed in the direction away from the equator.

[22] This study has been constructed using a quiet time plasma model [see *Li et al., 2010; Watt et al., 2012*]. Because quiet time parameters were used, wave growth is limited to large values of L . There are many variables in these plasma models, including the choice of the number of warm plasma components, and their variations in temperature, anisotropy, and density. It is likely that the predicted wave distributions will be sensitive to these choices, but it is important to base those choices on observations. Surveys like those published by *Li et al. [2010]* are therefore indispensable. Investigation of the sensitivity of the predicted wave distributions to the plasma parameters chosen is a formidable task, given the number of parameters involved, and will be reported in future work.

[23] An interesting alternate raytracing technique is presented in *Chen et al. [2013]* to study the power spectra of whistler-mode waves, specifically lightly damped chorus waves. The method presented by *Chen et al. [2013]* uses a prescribed source distribution of waves at the magnetic equator and predicts the wave spectra that result as the source waves are damped in their passage through the magnetosphere. The calculations presented in this paper are a method to predict the spectra of growing incoherent whistler-mode waves with no constraints placed on the original intensity or source of the waves. Both methods are nonlocal and follow waves with different characteristics as they move independently in both radial and latitudinal directions along different paths. The methods presented in *Chen et al. [2013]* and in this article are complementary and provide useful methods to track whistler-mode wave activity through the magnetosphere.

[24] The technique we have described can be used to make predictions of the wave distributions at any location, as long as the generated waves obey the caveats of quasilinear theory—i.e., they are incoherent and broadband—and have amplitudes that result in small perturbations in the plasma distribution function. The technique used in this paper cannot predict the wave distributions of whistler-mode chorus waves, since they most likely have a nonlinear generation mechanism [*Kato and Omura, 2007; Omura et al., 2008; Hikishima et al., 2009; Kato and Omura, 2011*]. These calculations are more relevant for prediction of the amplitude of “hiss-like” whistler-mode waves, similar to those observed and characterized in the equatorial plane by *Li et al. [2012]*. The backward raytracing technique can be used to predict the wave distributions of other types of electromagnetic wave that exhibit “ray” behavior and that are driven unstable by a relatively simple instability (e.g., anisotropy driven electromagnetic ion cyclotron waves) and so has more general utility.

[25] To obtain a prediction of the wave distribution, the plasma must be modeled not just at the observation location but in a volume of space surrounding the observation location that could support whistler-mode waves. Observational studies are required to constrain the energetic plasma components that contribute to wave growth (e.g., number density, temperature, and anisotropy). For example, it is unclear whether the simple model of warm plasma parameters as a function of latitude used in this paper and in *Watt et al. [2012]* is adequate for modeling the magnetosphere. Given observational surveys of energetic plasma over large regions of the magnetosphere, our new model can be validated with in situ observations of incoherent whistler-mode waves in different locations. Furthermore, the backward raytracing approach described in this paper offers the first step to constructing self-consistent kinetic models of whistler-mode wave-particle interactions over a large volume of the magnetosphere, where the balance between wave growth and particle diffusion could be studied more realistically.

6. Conclusion

[26] In this paper, we have introduced a methodology to construct the distribution of incoherent growing whistler-mode waves numerically from a combination of raytracing and solutions to the linear dispersion relation.

We describe how to combine the equations of radiation and geometric optics to predict all of the contributions to wave power at any particular location as a function of frequency and wavenormal angle. To demonstrate the capability of the technique, we show that in an idealized quiet time magnetosphere at 9 MLT and $L = 9$, the wave power peaks off the equator at 15° magnetic latitude. The wave spectral energy density can be approximated reasonably well with a Gaussian function, but the wavenormal distribution is best described by a skew normal distribution in wavenormal angle ψ , and most power lies in the wavenormals pointing away from the equator. The wave power does not peak at $\psi = 0, \pi$ (even at the equator), but at a small oblique angle that increases with latitude.

[27] As far as we are aware, this is the first time a methodology has been presented that allows the parallel and oblique incoherent wave spectrum to be calculated due to growing whistler-mode waves. It provides a means by which electron diffusion models can be made more self-consistent, by predicting the wave distributions as a function of plasma conditions, without having to run prohibitively expensive kinetic simulations.

[28] **Acknowledgments.** CEJW and AWD are supported by the Canadian Space Agency and NSERC, the Natural Science and Engineering Council of Canada.

References

- Bekefi, G. (1966), *Radiation Processes in Plasmas*, 377 pp., John Wiley and Sons, Inc., New York, NY, U.S.A.
- Beutier, T., and D. Boscher (1995), A three-dimensional analysis of the electron radiation belt by the Salammb code, *J. Geophys. Res.*, *100*, 14,853–14,861.
- Bortnik, J., U. S. Inan, and T. F. Bell (2006), Landau damping and resultant unidirectional propagation of chorus waves, *Geophys. Res. Lett.*, *33*, L03102, doi:10.1029/2005GL024553.
- Bortnik, J., R. M. Thorne, and N. P. Meredith (2007a), Modeling the propagation characteristics of chorus using CRRES suprathermal electron fluxes, *J. Geophys. Res.*, *112*, A08204, doi:10.1029/2006JA012237.
- Bortnik, J., R. M. Thorne, and N. P. Meredith (2007b), Ray tracing of penetrating chorus and its implications for the radiation belts, *Geophys. Res. Lett.*, *34*, L15109, doi:10.1029/2007GL030040.
- Bortnik, J., R. M. Thorne, and N. P. Meredith (2008), The unexpected origin of plasmaspheric hiss from discrete chorus emissions, *Nature*, *452*(7183), 62–66.
- Bortnik, J., L. Chen, W. Li, R. M. Thorne, and R. B. Horne (2011a), Modeling the evolution of chorus waves into plasmaspheric hiss, *J. Geophys. Res.*, *116*, A08221, doi:10.1029/2011JA016499.
- Bortnik, J., L. Chen, W. Li, R. M. Thorne, N. P. Meredith, and R. B. Horne (2011b), Modeling the wave power distribution and characteristics of plasmaspheric hiss, *J. Geophys. Res.*, *116*, A12209, doi:10.1029/2011JA016862.
- Chen, L., J. Bortnik, W. Li, R. M. Thorne, and R. B. Horne (2012a), Modeling the properties of plasmaspheric hiss: 1. Dependence on chorus wave emission, *J. Geophys. Res.*, *117*, A05201, doi:10.1029/2011JA017201.
- Chen, L., J. Bortnik, W. Li, R. M. Thorne, and R. B. Horne (2012b), Modeling the properties of plasmaspheric hiss: 2. Dependence on the plasma density distribution, *J. Geophys. Res.*, *117*, A05202, doi:10.1029/2011JA017202.
- Chen, L., R. M. Thorne, W. Li, and J. Bortnik (2013), Modeling the wave normal distribution of chorus waves, *J. Geophys. Res.*, *118*, doi:10.1029/2012JA018343, in press.
- Chum, J., and O. Santolik (2005), Propagation of whistler-mode chorus to low altitudes: Divergent ray trajectories and ground accessibility, *Ann. Geophys.*, *23*(12), 3727–3738.
- Chum, J., F. Jiricek, J. Smilauer, and D. Shklyar (2003), Magion 5 observations of chorus-like emissions and their propagation features as inferred from ray-tracing simulation, *Ann. Geophys.*, *21*(12), 2293–2302.
- Church, S. R., and R. M. Thorne (1983), On the origin of plasmaspheric hiss—Ray path integrated amplification, *J. Geophys. Res.*, *88*, 7941–7957.
- Fejer, J. A., and J. R. Kan (1969), Noise spectrum received by an antenna in a plasma, *Radio Sci.*, *4*, 721–728.
- Glauert, S. A., and R. B. Horne (2005), Calculation of pitch angle and energy diffusion coefficients with the PADIE code, *J. Geophys. Res.*, *110*, A04206, doi:10.1029/2004JA010851.
- Hikishima, M., S. Yagitani, Y. Omura, and I. Nagano (2009), Full particle simulation of whistler-mode rising chorus emissions in the magnetosphere, *J. Geophys. Res.*, *114*, A01203, doi:10.1029/2008JA013625.
- Horne, R. B., and R. M. Thorne (1997), Wave heating of He^+ by electromagnetic ion cyclotron waves in the magnetosphere: Heating near the H^+ - He^+ bi-ion resonance frequency, *J. Geophys. Res.*, *102*, 11457–11471.
- Huang, C. Y., and C. K. Goertz (1983), Ray-tracing studies and path-integrated gains of ELF unducted whistler mode waves in the earth's magnetosphere, *J. Geophys. Res.*, *88*, 6181–6187.
- Huang, C. Y., C. K. Goertz, and R. R. Anderson (1983), A theoretical study of plasmaspheric hiss generation, *J. Geophys. Res.*, *88*, 7927–7940.
- Inan, U. S., and T. F. Bell (1977), Plasmopause as a VLF wave guide, *J. Geophys. Res.*, *82*, 2819–2827.
- Katoh, Y., and Y. Omura (2007), Computer simulation of chorus wave generation in the Earth's inner magnetosphere, *Geophys. Res. Lett.*, *34*, L03102, doi:10.1029/2007GL0299758.
- Katoh, Y., and Y. Omura (2011), Amplitude dependence of frequency sweep rates of whistler-mode chorus emissions, *J. Geophys. Res.*, *116*, A07201, doi:10.1029/2011JA016496.
- Li, W., R. M. Thorne, N. P. Meredith, R. B. Horne, J. Bortnik, Y. Y. Shprits, and B. Ni (2008), Evaluation of whistler mode chorus amplification during an injection event observed on CRRES, *J. Geophys. Res.*, *113*, A09210, doi:10.1029/2008JA013129.
- Li, W., et al. (2009), Evaluation of whistler-mode chorus intensification on the nightside during an injection event observed on the THEMIS spacecraft, *J. Geophys. Res.*, *114*, A00C14, doi:10.1029/2008JA013554.
- Li, W., et al. (2010), THEMIS analysis of observed equatorial electron distributions responsible for the chorus excitation, *J. Geophys. Res.*, *115*, A00F11, doi:10.1029/2009JA014845.
- Li, W., R. M. Thorne, J. Bortnik, X. Tao, and V. Angelopoulos (2012), Characteristics of hiss-like and discrete whistler-mode emissions, *Geophys. Res. Lett.*, *39*, L18106, doi:10.1029/2012GL053206.
- Lyons, L. R., R. M. Thorne, and C. F. Kennel (1971), Electron pitch-angle diffusion driven by oblique whistler-mode turbulence, *J. Plasma Phys.*, *6*, 589–606.
- O'Hagan, A., and T. Leonard (1976), Bayes estimation subject to uncertainty about parameter constraints, *Biometrika*, *63*, 201–203.
- Omura, Y., Y. Katoh, and D. Summers (2008), Theory and simulation of the generation of whistler-mode chorus, *J. Geophys. Res.*, *113*, A04223, doi:10.1029/2007JA012622.
- Shprits, Y. Y., D. M. Subbotin, N. P. Meredith, and S. R. Elkington (2008), Controlling effect of the pitch angle scattering rates near the edge of the loss cone on electron lifetimes, *J. Atmos. Sol. Terr. Phys.*, *70*, 1694–1713.
- Su, Z., F. Xiao, H. Zheng, and S. Wang (2010), STEERB: A three-dimensional code for storm-time evolution of electron radiation belt, *J. Geophys. Res.*, *115*, A09208, doi:10.1029/2009JA015210.
- Thorne, R. M., S. R. Church, and D. J. Gorney (1979), Origin of plasmaspheric hiss—Importance of wave-propagation and the plasmopause, *J. Geophys. Res.*, *84*, 5241–5247.
- Watt, C. E. J., R. Rankin, and A. W. Degeling (2012), Whistler mode wave growth and propagation in the prenoon magnetosphere, *J. Geophys. Res.*, *117*, A06205, doi:10.1029/2012JA017765.